13th International Symposium on Turbulence and Shear Flow Phenomena (TSFP13)
Montreal, Canada, June 25–28, 2024

RESOLVENT ANALYSIS OF SEPARATED FLOWS OVER NACA0012 WINGS: REYNOLDS NUMBER EFFECTS

L. Victoria Rolandi, Luke Smith and Kunihiko Taira
Department of Mechanical and Aerospace Engineering
University of California, Los Angeles
vrolandi@ucla.edu, lsmith1@g.ucla.edu, ktaira@seas.ucla.edu

ABSTRACT

Separated flow over wings can lead to drag increase, lift decrease and aerodynamic efficiency reduction. In this study, we use biglobal and triglobal resolvent analysis (Trefethen *et al.*, 1993; Jovanović & Bamieh, 2005) to investigate how Reynolds numbers between 600 and 10,000 affect separated flows over two- and three-dimensional NACA0012 wings. It is essential to understand the effects of Reynolds numbers to accurately model and control turbulent flows. In particular, we focus on the similarities in separated flow structures across the range of Reynolds numbers. In this analysis, the base flow is the time-averaged flow obtained from direct numerical simulations and wall-resolved large eddy simulations. For the biglobal case, spanwise averaging is also applied. Particular emphasis is placed on uncovering the influence of the Reynolds number on the response and forcing modes as well as the energy gain associated with different frequencies.

RESOLVENT ANALYSIS

Let us consider the linear dynamics under forcing

$$\frac{\partial \mathbf{q}}{\partial t} = \mathscr{L}\mathbf{q} + \mathbf{f}, \tag{1}$$

where $\mathscr{L} \in \mathbb{R}^{n\times n}$ is the linearized Navier–Stokes operator about the time and spanwise-averaged base flow, $\mathbf{q} = (\rho, \rho\mathbf{u}, \rho e) \in \mathbb{R}^n$ is the state vector and $\mathbf{f} \in \mathbb{R}^n$ collects the nonlinear terms and the external forcing inputs (McKeon & Sharma, 2010). Here, n is proportional to the size of the spatial grid. The response ($\mathbf{q}$) and forcing ($\mathbf{f}$) can be decomposed through a temporal Fourier transform

$$\begin{aligned} \mathbf{q}(\mathbf{x},\mathbf{t}) &= \int_{-\infty}^{\infty} \hat{\mathbf{q}}_\omega(\mathbf{x}) e^{-i\omega t} d\omega, \\ \mathbf{f}(\mathbf{x},\mathbf{t}) &= \int_{-\infty}^{\infty} \hat{\mathbf{f}}_\omega(\mathbf{x}) e^{-i\omega t} d\omega \end{aligned} \tag{2}$$

providing for each angular frequency ω the following input-output relationship:

$$\hat{\mathbf{q}}_\omega(\mathbf{x}) = (-i\omega\mathbf{I} - \mathscr{L})^{-1}\hat{\mathbf{f}}_\omega(\mathbf{x}) = \mathbf{H}_\omega \hat{\mathbf{f}}_\omega(\mathbf{x}), \tag{3}$$

where $\mathbf{H}_\omega \in \mathbb{C}^{n\times n}$ is the resolvent operator that acts as a transfer function between the forcing and the response at frequency ω. Performing singular value decomposition of the resolvent operator, while retaining only the first $m \ll n$ singular values and singular right and left vectors, we find an approximation of $\mathbf{H}_\omega$:

$$\mathbf{H}_\omega \approx \mathbf{U}\Sigma\mathbf{V}^*. \tag{4}$$

Here, the columns of $\mathbf{U} = [\mathbf{u}_1, \mathbf{u}_2, ..., \mathbf{u}_m]$ and $\mathbf{V} = [\mathbf{v}_1, \mathbf{v}_2, ..., \mathbf{v}_m]$ represent the response and forcing modes, respectively, while $\Sigma = \mathrm{diag}(\sigma_1, \sigma_2, ..., \sigma_m)$ contains the gains of the corresponding forcing-response pairs, which maximize the energy norm (Chu, 1965; George & Sujith, 2011).

If the linear dynamics is unstable, we consider the discounted resolvent analysis (Jovanovic, 2004). In this case, the operator has the form:

$$\mathbf{H}_\omega = (-i\omega\mathbf{I} + \gamma - \mathscr{L})^{-1}, \tag{5}$$

where γ is the discount parameter that must satisfy $\gamma > \lambda_r$ with λ_r indicating the largest growth rate of $\mathscr{L}$. The discounted formulation is equivalent to considering the dynamics over a finite time horizon $t_\gamma = U_\infty 2\pi/c\gamma$, where U_∞ is the freestream velocity and c the chord of the wing.

COMPUTATIONAL SET-UP

Biglobal

We simulate the spanwise periodic flow around a NACA0012 airfoil at an angle of attack of 14° for Reynolds numbers within the range $Re \in [1000; 10000]$ and Mach number $M_\infty = 0.1$. The base flows, averaged over time and in the spanwise direction, are simulated with direct numerical simulations (for $Re \leq 2500$) and wall-resolved large eddy simulations (for $Re > 2500$), for which we employ the Vreman subgrid-scale model (Vreman, 2004). A spanwise domain length L_z of one airfoil chord length is used to capture three-dimensional features in the simulations. The nonlinear simulations use a no-slip adiabatic boundary condition on the surface of the airfoil, uniform constant velocity, pressure, and temperature at the inlet and on the upper and lower sides, a zero-pressure-gradient at the outlet, and periodic boundary conditions on the lateral sides. The direct numerical simulations conducted at $Re = 1000$ are verified with previous works (Gupta *et al.*, 2023; Rolandi *et al.*, 2022).

Triglobal

We also simulate the three-dimensional flow around a NACA0012 finite wing with a semi-aspect ratio of $sAR = 2$

Figure 1. Instantaneous spanwise periodic flow around a NACA0012 airfoil at $\alpha = 14^\circ$ and different Reynolds numbers. Flow field visualized with isocontour of Q-criterion colored by streamwise velocity.

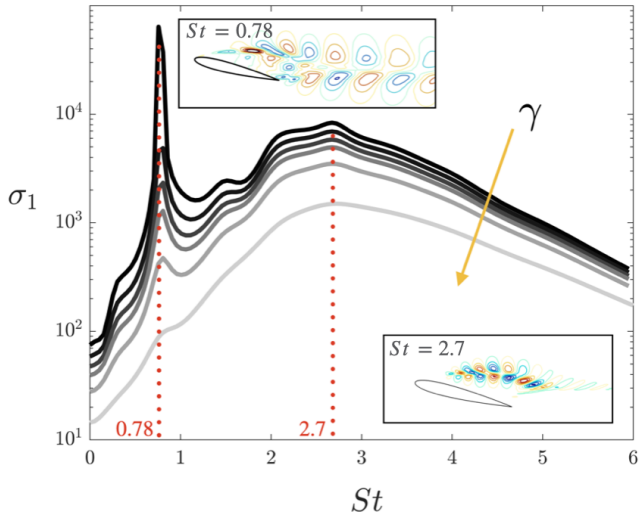

Figure 2. Gain variation over forcing frequency at $Re = 10000$. Influence of discount parameter γ on σ_1 illustrated in grayscale. Response mode at $St = 0.78$ and 2.7 considering $t_\gamma = 41$ visualized with isocontours of streamwise velocity.

at an angle of attack of $\alpha = 14^\circ$ for $Re \in [600;2500]$ and $M_\infty = 0.1$. The wing features a rounded tip. The boundary conditions for the nonlinear simulations include a no-slip adiabatic boundary condition on the wing surface, uniform constant velocity, pressure, and temperature at the inlet, a sponge condition at the outlet and a symmetry condition at the wing root ($z = 0$) allows for the simulation of only half of the computational domain.

To conduct the biglobal resolvent analysis, the time- and spanwise-averaged base flow is interpolated onto a two-dimensional grid, whereas for the triglobal analysis, the time-averaged base flow is interpolated onto a three-dimensional grid. The interpolated base flows are then used to compute the linear operator. The singular value decomposition of the resolvent operator is performed using Krylov subspace projection methods. Since the linear operator exhibit unstable leading eigenvalues, discounted resolvent analysis is considered. Both the calculation of the base flow and resolvent analysis are performed with the compressible flow solver CharLES (Khalighi *et al.*, 2011) coupled with the PETSc and SLEPc libraries (Balay *et al.*, 2020; Roman *et al.*, 2016) for performing the singular value decomposition.

BIGLOBAL RESOLVENT ANALYSIS

The unsteady spanwise periodic flows of the cases studied are illustrated in Fig. 1. At an angle of attack of 14° and a Reynolds number of $Re = 1000$, the flow has transitioned to a three-dimensional flow with a characteristic spanwise length of approximately $\approx c/3$. As the Reynolds number increases, the characteristic spanwise wavelength shortens and the flow becomes progressively more chaotic.

Discount Effects

Fig. 2 presents the gain variation of the first singular value as a function of the forcing frequency $St = \omega/2\pi$ at $Re = 10000$ and spanwise wavenumber $\beta = 0$ for different discount parameters corresponding to $t_\gamma \in [5;41]$. The variation of the discount parameter γ reveals two distinct peaks: one at $St \approx 2.7$ and the other at $St \approx 0.78$. The peak at $St \approx 2.7$ is associated with shorter finite horizon times (larger γ values), reflecting early dynamics. From the modal structure depicted in the bottom right of the figure, we can see that this frequency is linked to flow mechanisms within the separated shear region. The second peak, at $St \approx 0.78$ arises at longer horizon time t_γ. Indeed, this frequency also corresponds to the frequency of the leading eigenvalue computed from linear stability analysis. From the modal structure at $St \approx 0.78$, we observe that this frequency is linked to the wake dynamics. For the subsequent analysis, we employ a discount parameter of $\gamma = 1.2$.

Reynolds number effects

In Fig. 3, the streamwise velocity fields of the response and forcing modes, along with the wavemaker of the first singular modes, are depicted for Reynolds numbers $Re = 1000$ and 10000. The wavemaker is calculated as the dot product between the response and forcing modes. At the lowest frequency, there is a significant difference between the two Reynolds numbers in the three flow fields presented. Particularly, the higher Reynolds number exhibits a thinning of mode structures over the base flow shear layer, which remains evident in the response mode flow field up to $St \approx 1$. Despite the differences in the shear layer, the response modes for both cases share similarities in the wake region for Strouhal numbers $St \leq 1$. As St increases, both response mode structures shift toward the shear layer regions, displaying greater similarities within this region. The similarities in the response modal structures at constant forcing frequency across the Reynolds numbers originate from the characteristic streamwise wavelength in the modal structures which strongly correlates to the forcing frequency.

For the Strouhal number range considered, there is important difference in the forcing modes. At the higher Reynolds number, the forcing mode develops upstream, whereas at the lower Reynolds number case, the forcing mode structures are more concentrated in the shear layer region. This difference is also evident in the wavemaker flow field, which indicates the overlap of the response and forcing mode pairs. For the higher Reynolds number case, elongated thin predominant structures are observed over the shear layer and they weaken as St increases. In contrast, for the lower Reynolds number case, the

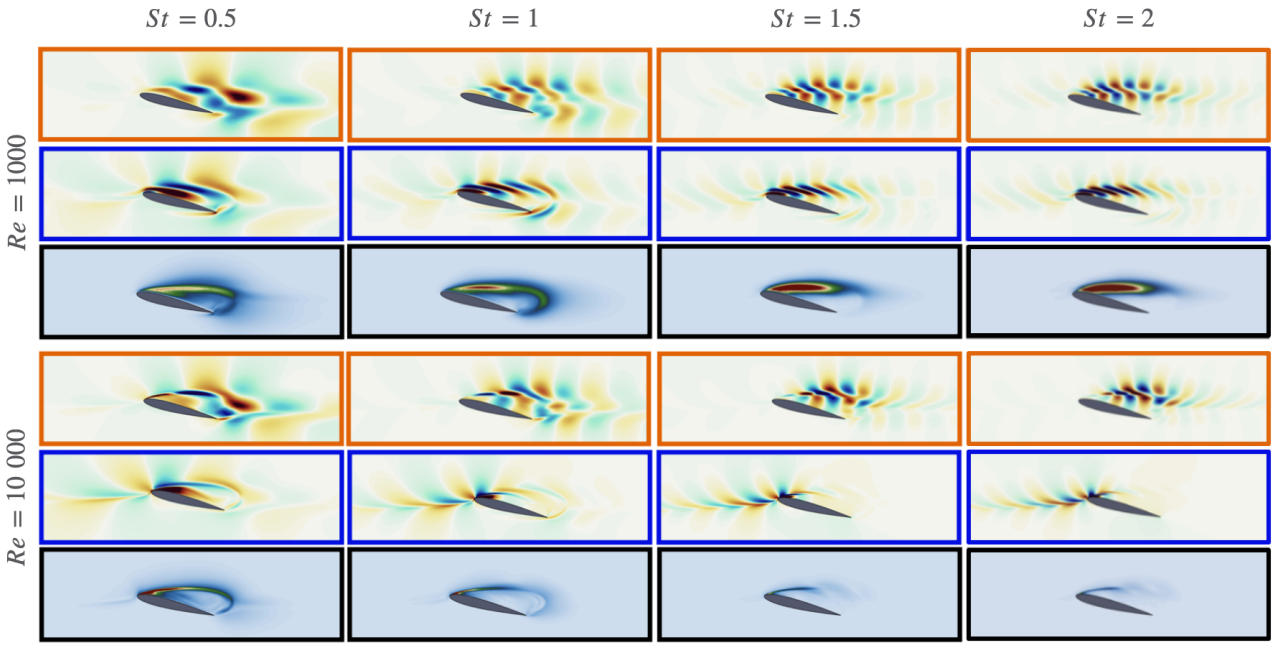

Figure 3. The primary streamwise velocity response modes (orange frames), streamwise velocity forcing modes (blue frames) and wavemakers (black frames) at spanwise wavenumber $\beta = 0$, Reynolds numbers $Re = 1000$ and 10000 over different Strouhal numbers.

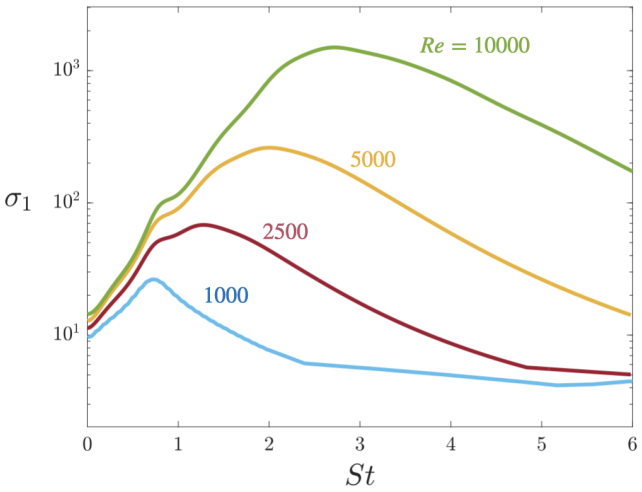

Figure 4. Gain distribution over frequency at different Reynolds numbers and spanwise wavenumber $\beta = 0$.

wavemaker intensifies in the shear layer.

The gain distribution over the forcing frequency for different Reynolds numbers is illustrated in Fig. 4. As the forcing frequency increases, the maximum gain also rises, though the peak becomes less pronounced with higher Reynolds numbers. The bump observed around $St \approx 0.7$ for $Re \geq 2500$ and the highest peak at $Re = 1000$ correspond to frequencies associated with the leading eigenvalue of the linear operators.

The influence of spanwise wavenumber β on gain distribution is illustrated in Fig. 5. In this figure, we show the gain distributions for the leading three singular values (σ_1, σ_2, and σ_3) on the $\beta - St$ plane for Reynolds numbers $Re = 1000$ and 10000. For reference, the shedding frequencies (peak frequencies of the lift coefficient spectra) are also marked with black dashed lines. In both Reynolds number cases, the overall distributions of σ_1, σ_2, and σ_3 display similarities. For σ_1, the maximum gain occurs at $\beta = 0$, with a slight increase in gain at the lowest Strouhal number for the $Re = 1000$ case at $\beta \approx 3\pi$. In contrast, σ_2 shows a peak at $\beta \approx 2\pi$ for both Reynolds numbers. The peak shifts toward lower Strouhal numbers as β increases. A similar trend is observed for σ_3, where again the peak shifts toward lower Strouhal numbers as β increases. In the $Re = 1000$ case, the gain peaks of σ_1 and σ_2 align with the shedding frequency. However, in the $Re = 10000$ case, only the maximum of σ_2 and σ_3 align with the shedding frequency, while σ_1 aligns with frequencies related to the shear mechanisms, exhibiting a maximum at higher St. This is due to the fact that shear regions are known to host nonmodal growths (Schmid, 2007). Therefore, over short time, we observe higher gain from these mechanisms.

TRIGLOBAL RESOLVENT ANALYSIS

The instantaneous flow fields for the cases studied are presented in Fig. 6. As the Reynolds number increases, the spanwise length scales of the flow structures within the wake become shorter.

Reynolds number effects

Figure 7(a) illustrates the gain variation of the three leading singular values over the forcing frequencies. The gain increases with the Reynolds number, and similarly to the biglobal case, the frequency at which maximum gain occurs also rises. Additionally, the frequency of the maximum gain shows slight variations among the three singular values (σ_1, σ_2 and σ_3) at fixed Reynolds number and they are in the same order of magnitude. This is different from the biglobal case, where the the first singular value σ_1 was significantly larger compared to the higher order singular values, σ_2 and σ_3.

Figure 7(b) presents the streamwise velocity contours of the forcing and response modes for $Re = 600$ and 2500 at the different forcing frequencies highlighted in Fig. 7(a). The black dotted line marks the centerline at the root of the wing

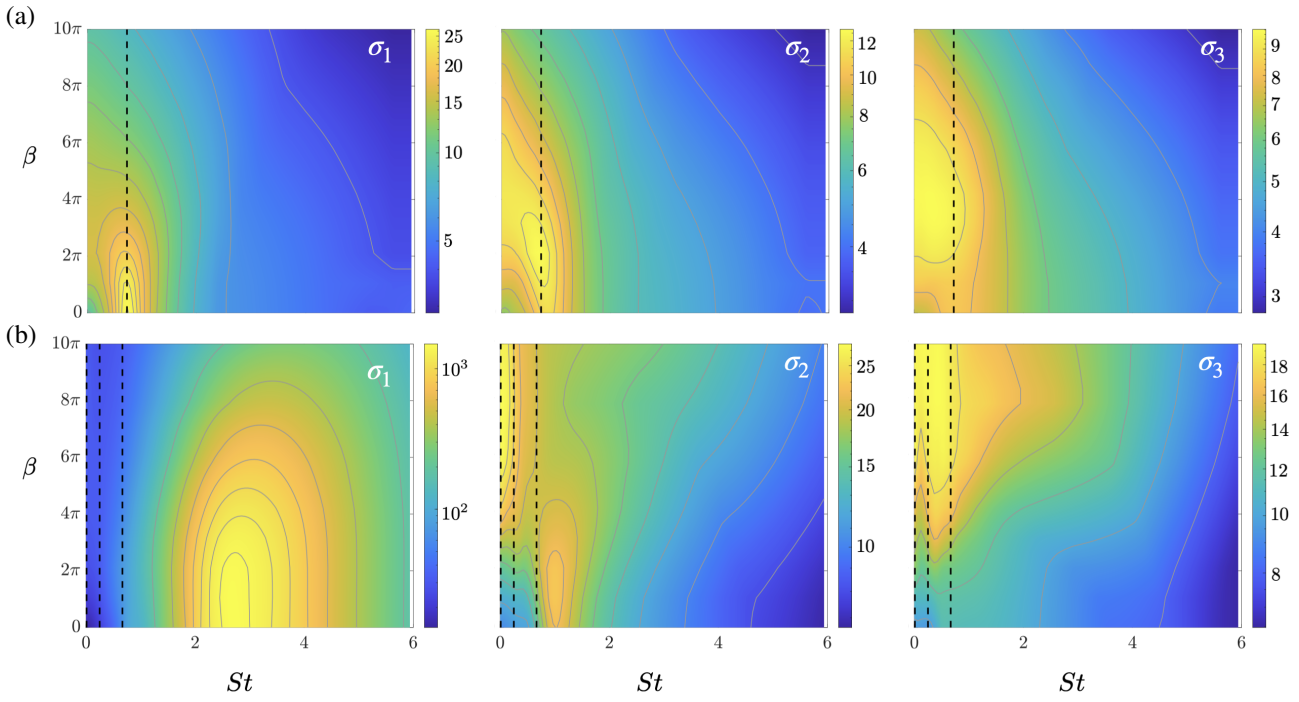

Figure 5. Distributions of the first three dominant gains over the $\beta - St$ plane at (a) $Re = 1000$ and (b) $Re = 10000$. Black dashed lines indicate the dominant frequency peaks associated with lift coefficients.

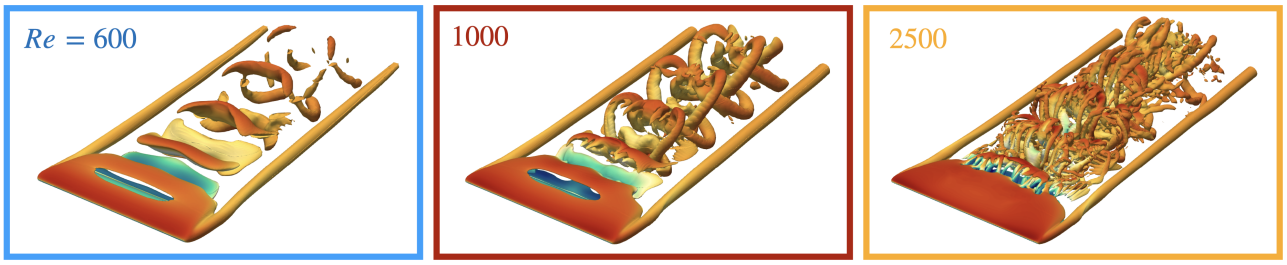

Figure 6. Iso-surface of Q-criterion colored by streamwise velocity of the flow around a finite wing of semi-aspect ratio $sAR = 2$ at $\alpha = 14°$ and $Re = 600$, 1000 and $Re = 2500$.

at $z = 0$. As the forcing frequency increases, the characteristic length of the modal structure shorten.

By examining the spanwise positions of maximum intensity for the forcing and response modes, we find that at the lowest Reynolds number, the response mode is inboard relative to the forcing mode, indicating a misalignment between the two. However, as the Reynolds number increases, the forcing and response modes become aligned along the streamwise direction. For both scenarios, an increase in forcing frequency shifts the forcing and response modes from the inboard region toward the outboard region, in agreement with findings at lower Reynolds numbers from Ribeiro *et al.* (2023). In particular, for the $Re = 2500$ case, we observe the forcing and response structures shifting in the tip region.

The modal structures also exhibit a sweep relative to the wing-span. This angle is denoted as Λ and is measured on the xz-plane at $y = 0$. The variation of Λ is shown in Fig. 8 for $Re = 600$ and 2500. At a forcing frequency of $St = 0$, the modal structures align with the streamwise direction, $\Lambda = 90°$. As the forcing frequency increases, Λ decreases. For both Reynolds numbers, the frequency at which $\Lambda = 0°$ corresponds to the frequency of maximum gain ($St \approx 0.6$ for $Re = 600$ and $St \approx 1.1$ for $Re = 2500$), revealing that structures parallel to the wing-span are those that are the most amplified. As the forcing frequency continues to rise, the angle becomes negative, with the modal structures moving towards the tip region.

The variation of Λ also highlights the mode switching over the forcing frequency. In the $Re = 2500$ case, indeed, we observe a clear discontinuity at $St \approx 2$, which is associated with mode switching. Tip vortex mode structures show a sweep angle of $\Lambda = 45°$. Another discontinuity along the variation of the sweep angle variation occurs at $St = 0.5$ for both Reynolds numbers. Notably, this frequency might be related to the semi-aspect ratio length (as $sAR = 2 = 1/0.5$). However, further exploration of other aspect ratios is needed to confirm this assumption.

CONCLUSIONS

In this study, we perform biglobal and triglobal resolvent analysis to investigate the effects of Reynolds number on the separated flow around two- and three-dimensional NACA0012 wings at an angle of attack 14°. Energy gains and mode structures are computed at different forcing frequencies and compared with respect to the Reynolds number.

In the biglobal case, the modes present prevalent shear-region or wake-region structures depending on the forcing frequency. Also, we find similarities in the response modal

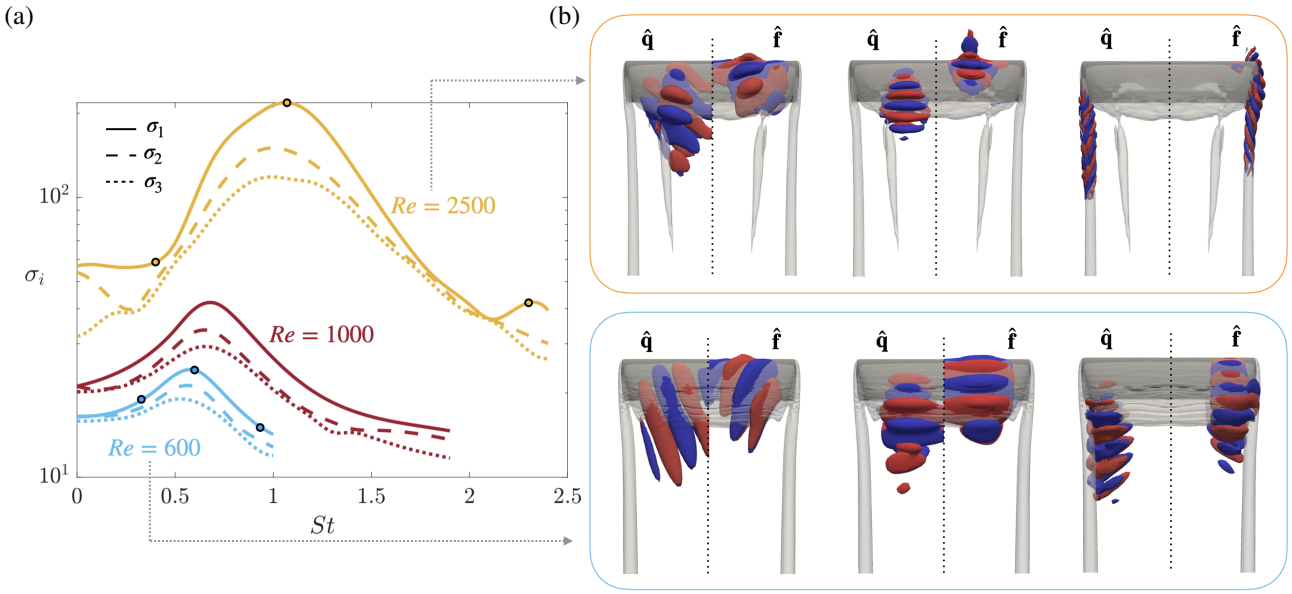

Figure 7. (a) Variation of the first three dominant gains over forcing frequency at different Reynolds numbers. (b) First response and forcing modes at frequencies indicated by the dots in (a) for Reynolds number $Re = 600$ and 2500. Visualization of isosurfaces of streamwise velocity superposed to translucent isosurface of Q-criterion of the base flow.

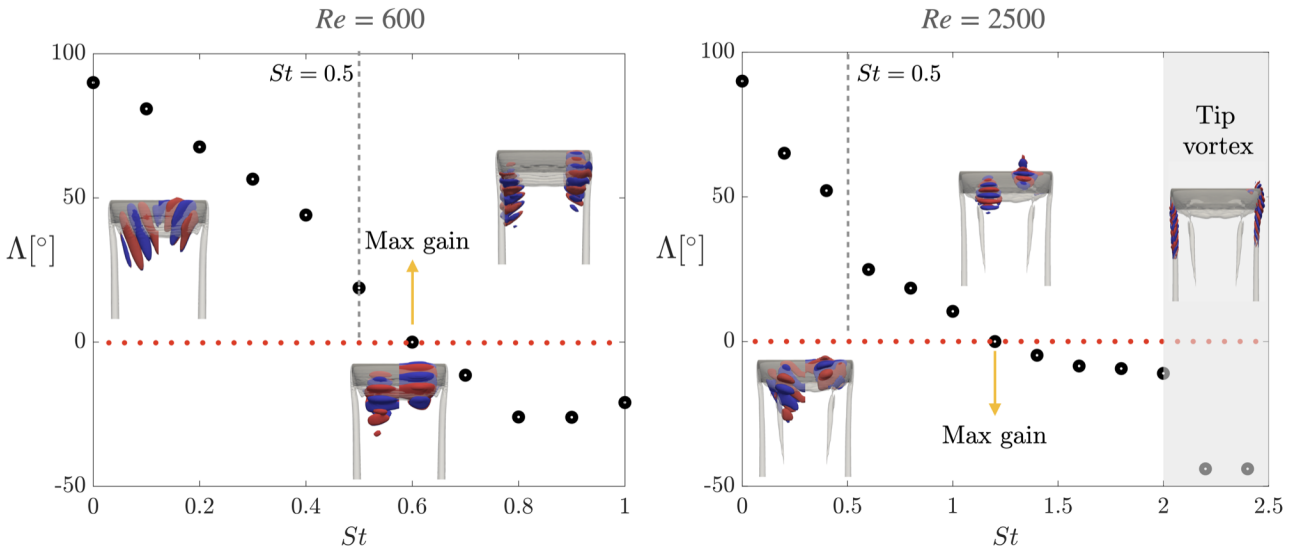

Figure 8. Sweep angle of the forcing and response mode structure with respect to the wing-span. Variation over forcing frequency at Reynolds numbers $Re = 600$ and 2500.

structures at the same forcing frequencies, due to the fact that the characteristic streamwise wavelength only depends on the forcing frequency and not on the Reynolds number. However, the forcing modes are different among the Reynolds numbers considered, since they tend to develop upstream as the Reynolds number is increased, due to the convective nature of these modes.

In the triglobal resolvent analysis, the modes are characterized by finer structures as they move outboard toward the tip vortex region. Also, we find that the sweep angle of the modal structures with respect to the wing-span is strongly correlated with the maximum gain. For all Reynolds numbers considered, the maximum gain is indeed achieved by structures that are parallel to the wing-span direction.

As a continuation of this study, we aim to extend the triglobal resolvent analysis to higher Reynolds number cases, and possibly investigate different semi-aspect ratios and swept wings.

FUNDING

This work was supported by the U.S. Army Research Office (Grant Number W911NF-21-1-0060) and U.S. Air Force Office of Scientific Research (Grant Number FA9550-21-1-0174).

ACKNOWLEDGMENT

This work used computational and storage services hosted by the Hoffman2 Shared Cluster at UCLA's Institute for Digital Research and Education's Research Technology Group.

REFERENCES

Balay, Satish, Abhyankar, Shrirang, Adams, Mark F, Brown, Jed, Brune, Peter, Buschelman, Kris, Dalcin, Lisandro, Dener, Alp, Eijkhout, Victor, Gropp, W *et al.* 2020 Petsc users manual (rev. 3.13). *Tech. Rep.*. Argonne National Lab.(ANL), Argonne, IL (United States).

Chu, Boa-Teh 1965 On the energy transfer to small disturbances in fluid flow (Part I). *Acta Mechanica* **1** (3), 215–234.

George, K Joseph & Sujith, RI 2011 On Chu's disturbance energy. *Journal of Sound and Vibration* **330** (22), 5280–5291.

Gupta, Siddharth, Zhao, Jisheng, Sharma, Atul, Agrawal, Amit, Hourigan, Kerry & Thompson, Mark C 2023 Two- and three-dimensional wake transitions of a naca0012 airfoil. *Journal of Fluid Mechanics* **954**, A26.

Jovanovic, Mihailo R 2004 *Modeling, analysis, and control of spatially distributed systems*. University of California, Santa Barbara.

Jovanović, Mihailo R & Bamieh, Bassam 2005 Componentwise energy amplification in channel flows. *Journal of Fluid Mechanics* **534**, 145–183.

Khalighi, Yaser, Ham, Frank, Nichols, Joseph, Lele, Sanjiva & Moin, Parviz 2011 Unstructured large eddy simulation for prediction of noise issued from turbulent jets in various configurations. In *17th AIAA/CEAS aeroacoustics conference (32nd AIAA aeroacoustics conference)*, p. 2886.

McKeon, Beverley J & Sharma, Ati S 2010 A critical-layer framework for turbulent pipe flow. *Journal of Fluid Mechanics* **658**, 336–382.

Ribeiro, JH Marques, Yeh, Chi-An & Taira, Kunihiko 2023 Triglobal resolvent analysis of swept-wing wakes. *Journal of Fluid Mechanics* **954**, A42.

Rolandi, Laura Victoria, Jardin, Thierry, Fontane, Jérôme, Gressier, Jérémie & Joly, Laurent 2022 Stability of the low reynolds number compressible flow past a NACA0012 airfoil. *AIAA Journal* **60** (2), 1052–1066.

Roman, Jose E, Campos, Carmen, Romero, Eloy & Tomás, Andrés 2016 Slepc users manual. *D. Sistemes Informàtics i Computació, Universitat Politècnica de València, TR DSIC-II/24/02, Rev* **3**.

Schmid, Peter J. 2007 Nonmodal stability theory. *Annual Review of Fluid Mechanics* **39**, 129–162.

Trefethen, Lloyd N, Trefethen, Anne E, Reddy, Satish C & Driscoll, Tobin A 1993 Hydrodynamic stability without eigenvalues. *Science* **261** (5121), 578–584.

Vreman, AW 2004 An eddy-viscosity subgrid-scale model for turbulent shear flow: Algebraic theory and applications. *Physics of fluids* **16** (10), 3670–3681.